Prediction of STS-107 Hypervelocity Flow Fields about the Shuttle Orbiter with Various Wing Leading Edge Damage

Maria V. Pulsonetti, Richard A. Thompson, Stephen J. Alter
NASA Langley Research Center, Hampton, Virginia

Abstract

Computations were performed for damaged configurations of the Shuttle Orbiter in support of the STS-107 Columbia accident investigation. Two configurations with missing wing leading-edge reinforced carbon-carbon (RCC) panels were evaluated at conditions just prior to the peak heating trajectory point. The initial configuration modeled the Orbiter with an approximate missing RCC panel 6 to determine whether this damage could result in anomalous temperatures measured during the STS-107 reentry. This missing RCC panel 6 computation was found to produce heating augmentation factors of 5 times the nominal heating rates on the side fuselage with lesser heat increases on the front of the OMS pod. This is consistent with the thermocouple and resistance temperature detector sensors from the STS-107 re-entry which observed off nominal high early in the re-entry trajectory. A second damaged configuration modeled the Orbiter with missing RCC panel 9 and included ingestion of the flow into the outboard RCC channel. This computation lowered the level (only 2 times nominal) and moved the location of the heating augmentation on the leeside fuselage relative to the missing RCC panel 6 configuration. The lesser heating augmentation for missing RCC panel 9 was confined near the wing fuselage juncture. Near nominal heating was predicted on the remainder of the side fuselage with some lower than nominal heating on the front surface of the OMS pod. These results for missing RCC panel 9 are consistent with data from the STS-107 re-entry where the heating augmentation was observed to move off the side fuselage and OMS pod sensors at later times in the trajectory. As this solution requires supersonic mass ingestion into the RCC channel, it is probably not an appropriate model prior to penetration of the flow through the spar into the wing structure. It may, however, be representative of the conditions at later times and could account for the movement of the heating signature on the side fuselage.

Introduction

Members of the Aerothermodynamics Branch at NASA Langley Research Center (LaRC) began investigation of the aerothermodynamic environment of the STS-107 Orbiter immediately following the accident on February 1, 2003. Computations supported the ground based experimental investigations in fluid dynamics and aeroheating (Horvath, 2003), aerodynamics (Brauckmann, 2003), and damaged tile (Everhart, 2003). At that time, a parallel computational effort using both inviscid (Bibb, 2003) and viscous analyses to simulate damage to the Shuttle Orbiter at flight conditions was started. The viscous computational simulations are the focus of this report.

At the outset of the STS-107 investigation it was known from telemetry data that off-nominal high temperatures had been measured by bondline (backside) resistance temperature

Aproved for public release; distribution is unlimited

detectors (RTD's) located on the side fuselage above the Orbiter wing, as shown in Figure 1. It was not known at the time whether these temperature rises were caused by aerodynamic heating from the external flow field or by sources internal to the vehicle structure. If the cause was external, then a general consensus existed that damage to the wing leading edge would be the most probable mechanism for flow field alteration leading to an increased heating on the upper side fuselage. This reasoning led to modeling the loss of leading-edge reinforced carbon-carbon (RCC) panels along the Orbiter wing leading edge. Figure 2 shows the layout of these 21 RCC leading edge panels. Two damaged geometries were considered in this work. The first configuration was an approximation of a missing RCC panel 6 (herein referred as panel 6 "notch") where the sides of the notch were solid allowing no mass ingestion into the structure. The second configuration simulated a complete missing RCC panel 9 with flow ingestion into the RCC channel. These studies were focused on reentry times just prior to the start of peak heating conditions where the external flow is characterized by high angle of attack, hypervelocity conditions. These cases and the results observed from the computations are described more fully in the following sections.

LAURA Conditions

The computations were performed using the Langley Aerothermodynamic Upwind Relaxation Algorithm (LAURA) code (Gnoffo et al.,.1989, Gnoffo, 1990). LAURA is a high fidelity analysis tool, specialized for hypersonic re-entry physics, utilizing state-of-art algorithms for computational fluid dynamic (CFD) simulations. The computations were performed using a thin layer formulation of the Navier Stokes equations. The flight computations assumed the flowfield to be laminar, in chemical nonequilibrium (5 reacting species), and thermal equilibrium. All solid surfaces were treated as partially catalytic to recombination using the reaction rates for reaction cured glass (RCG) from Stewart (1997). Radiation equilibrium of the wall was assumed to calculate the wall temperature with a surface emissivity of 0.89.

Both damage configuration CFD solutions were obtained at a condition referenced as Case 1 on the STS-107 trajectory. The time from entry interface (EI) was 404 sec and the Orbiter was at an altitude of 74.081 km. The freestream Mach number was 24.83 and the angle of attack of 40.17 degrees.

RCC Panel 6 "Notch"

Very little information existed at the start of the investigation to guide the assessment of various failure scenarios. The decision to consider a missing RCC panel was clear but the choice of which panel and the exact geometry was not. Early in the investigation, prior to the MADS data recovery, the primary sensors that measured off-nominal high temperatures and failed during reentry were located in the port wheelwell. It was assumed that damage to the leading edge near the forward outboard corner of the wheelwell was likely based on its proximity. RCC panel 6 was the leading edge panel closest to this region (Figure 3). In addition, early predictions of the foam strike on the left wing performed by the Intercenter Photo/Image Working Group indicated that the region of RCC panels 5, 6 and 7 was the most probable damage location as shown in Figure 4. Thus, it was thought most appropriate to model a missing RCC panel 6 in an attempt to reproduce the heating augmentation on the side fuselage and to quantify the local heating to the main wing spar exposed by the missing RCC panel.

For expediency, an existing CFD surface and volume grid was modified to simulate the damaged geometry. The coordinates that define RCC panel 6 were estimated from existing literature since this work occurred prior to acceptance and distribution of a common CAD geometry within the investigation team. Subsequent comparison of the estimated panel 6 coordinates with the actual size and location revealed that the approximated missing panel was centered about the correct location but was only roughly 2/3 of the full size. Figure 5 shows a planform view of the missing panel modeled in this work compared to the size and location of the actual RCC panels. To construct the missing panel geometry, solid vertical surfaces were used

to slice the nominal Orbiter geometry along the sidewalls and backplane thereby forming the leading edge cavity. In reality, the sidewalls of a cavity formed by a missing RCC panel are hollow which would allow flow into the channel on either side, but the channel was not modeled in this computation. The backplane of the cavity is a rough approximation of the main wing spar in this simulation; however, no other internal geometry (e.g. spanner bars, carrier panels, earmuffs) was modeled.

The CFD grid about the vehicle and inside the cavity used in these computations is shown in Figure 6. The grid about the vehicle, using the 1997 geometry definitions, consisted of three sections; forebody, midbody, and aftbody. The midbody grid, shown in black, was regenerated using an embedded O-grid topology to allow the clustering of grid points towards the hole created by the missing RCC panel while not requiring grid density increases on the vehicle wing or nose. A grid was constructed in the cavity of the missing RCC panel using a second embedded O-grid topology which allows clustering of grid cells against the solid side and back surfaces to capture viscous boundary-layer behavior. The interior cavity grid was composed of 5 matching blocks surrounding the O-grid structure (Alter, 2003). A solution was obtained on a grid with about 8.5 million points of which 2.5 million were located within the missing RCC panel cavity.

Figure 7 shows one aspect of the resulting flow solution where a slice that crosses the RCC cavity has been extracted in the planform plane. The density contours for both the smooth outer mold line (OML) geometry and the case of missing RCC panel 6 notch are shown. The higher density zone on the smooth OML indicates the location of the shock-shock interaction where the bow shock off the nose interacts with the shock off the wing leading edge. It is clear that panel 6 is inboard of the shock-shock interaction. The boundary layer thickness for the flow approaching the cavity varied from 0.9 inches at the wing leading edge to 1.7 inches at the inboard windside corner of the notch. The unit Reynolds number varied from 4500/ft at the wing leading edge and 6100/ft at the inboard windside corner of the cavity. For the damaged configuration, shock waves are anchored at both the inboard and outboard leading-edge corners of the cavity. These embedded shocks are formed around the recirculating flow within the cavity at the inboard corner and from impingement of flow on the outboard corner. Both shocks form weak interactions with the wing bow-shock downstream of the cavity. By comparison of the smooth OML and the damaged configuration, there appears to be a very small effect on the outer bow shock and downstream flow in this plane with the presence of the cavity. The only differences noted are the additional features described for the missing panel case. This observation regarding the downstream flow also held true for other planes around the leading edge.

The streamlines in the vicinity of the missing portion of RCC panel 6 are shown in Figure 8. The streamlines in the cavity are volume streamlines, except near the leading edge of the outboard sidewall where the formation on an attachment line is shown. Streamlines outside the cavity are on the surface. The streamlines that enter the notch strike the outboard sidewall and some are turned upward to exit at the outboard leeside edge of the cavity. These streamlines then travel toward the fuselage but never strike it. The remaining streamlines hitting the outboard side of the cavity twist in a vortical pattern striking the inboard side of the cavity. They then exit on the inboard leeside corner of the cavity and eventually strike the fuselage. The surface streamlines on the upper wing surface ahead of the notch show that a separation line is formed by the presence of the flow exiting the cavity. This leeside flow separation extends to near the side fuselage before turning downstream to mix with the flow that scrubs the side of the fuselage.

The heat flux in the cavity created by the missing portion of RCC panel 6 is shown in Figure 9. The peak heating within the cavity occurs on the outboard sidewall of the cavity where heat flux values as high as 118 BTU/ft^2/s are predicted (roughly 3 times the nominal peak wing leading edge heating). This high heating is due to the large gradients present in the thin boundary layer formed as the flow expands from the attachment line in the cavity around the corner onto the wing leading edge. The flow that strikes the windside edge of the outboard cavity

is redirected to the backwall of the cavity starting the formation of a weak vortex within the cavity. High heating is observed on the backwall of the cavity near the sidewall where a heat flux of 117 BTU/ft^2/s is predicted.

The streamlines which exit the notch are shown in Figure 10. As discussed in the previous figure, the streamlines exiting the outboard corner of the notch travel upward and toward the body but never strike the surface. The streamlines exiting the inboard leeside corner of the notch travel in a more direct path toward the fuselage and strike the side of the fuselage. They are then turned downstream and form a weak vortex of hot gas which originated from the windside and scrubs the side of the fuselage.

While the effect of the missing panel 6 “notch” was minimal along the wing leading edge, its impact was very evident in the wing leeside flow. Figures 11 -13 show the temperature contours plotted in vertical planes that have been extracted from the flow field at three axial stations (at the missing panel 6 “notch”, midway between panel 6 and the OMS pods, and at the front face of the OMS pods). These figures compare the flow fields of the nominal (i.e. non damaged) Orbiter geometry with the flow field predicted on the leeside with missing RCC panel 6. The sequence of figures shows the jet flow out of the cavity and directed toward the side fuselage and then the progression of this flow down the fuselage. In probing the computed flow field, this jet flow was found to leave the cavity and travel almost transversely toward the symmetry plane where it impacted the fuselage at a nearly perpendicular angle. At the fuselage, the flow is turned abruptly downstream. The accompanying temperature increase in the flow field is due to both the hot gas flowing from the windside and the impact of this jet on the fuselage.

The effect of the irregular flow on the orbiter leeside is most evident in the surface pressure and heating experienced on the side fuselage. Figures 14 and 15 illustrate these effects by showing contours of the increase in predicted surface pressure and heating rate over the nominal case. The pressure effect is computed as a difference in Cp and the effect on heat transfer is shown as a ratio of off-nominal to nominal heating. The area of pressure and heating increases are located almost directly transverse to the missing RCC panel 6. Both areas show an angled orientation sloping upward and aft. The maximum heating augmentation from the current prediction is approximately 5 times the nominal rate. The effect of the increased heating rate on the equilibrium surface temperature is presented in Figure 16. Here, the absolute difference in temperature between the nominal and missing RCC panel solution is shown. The peak temperature produced on the side fuselage for the damaged case is 732 deg F which is near the limit for the TPS blankets in this region.

A qualitative comparison of the computed heating augmentation of the side fuselage with a measured wind tunnel heating image (Horvath, 2003) is shown in Figure 17. The heating image was obtained using a phosphor thermography technique (Buck, 1989; Merski, 1998a-b) in the LaRC CF_4 tunnel for an Orbiter model with a similar missing RCC panel 6. It’s important to note that the computed heating augmentation is the change in heat flux of the damaged Orbiter configuration relative to the undamaged configuration whereas the thermographic phosphor image obtained in the wind tunnel shows the non-dimensional heat transfer coefficient ratio. A qualitative comparison of the two images show a comparable heating footprint on the Orbiter side fuselage in terms of both location and orientation. Heating augmentation on the front of the OMS pod is also observed in the thermographic phosphor image. The other heating regions observed on the experimental image do not represent augmented heating.

The flight data recorder (or MADS data) was recovered subsequent to obtaining the prediction for missing RCC panel 6. Figure 18 shows some of these MADS surface thermocouple readings from the left side fuselage and the left OMS pod as a function of time. The orange and blue lines represent side fuselage measurements that were observed to behave with off-nominal high readings between 560 to 620 seconds EI. These surface thermocouple measurements reinforced the evidence for external heating of the side fuselage beyond the

original telemetry (bondline/backside) data. A better understanding of the timing and location of heating augmentation (or reduction) was also gained from this additional data.

Missing RCC Panel 9 with Unrestricted Ingestion into RCC Channel

Following analysis of the MADS data and debris recovery, the investigating team were led to believe that a more likely damage was the loss of an RCC panel in the vicinity of panel 9. This reasoning was based on a number of factors. First, no pieces of RCC panel 9 were recovered except the ribs on the sides of the panel. This is shown in Figure 19 where the debris in the vicinity of RCC Panel 9 is compiled. Also, the debris forensics indicated that the windside carrier panels downstream of RCC panel 9 showed considerable slumping indicative of exposure to temperatures above 3000 deg F for several minutes. The leeside carrier panels also showed evidence of prolonged exposure to temperatures above 3000 deg F. In addition, the computational team was concerned about the level of accuracy in modeling the Panel 6 notch as the ingestion of mass into the structure had not been considered. Therefore, a computational analysis of the flowfield effects from the loss of RCC panel 9 on the orbiter was performed using the LAURA code. For this analysis, gas entering the cavity formed by the missing RCC panel was allowed to flow into the outboard RCC channel by imposing vacuum conditions on the sidewall. In actuality, however, the solution is independent of the back pressure in the channel so long as the back pressure is low enough to produce supersonic flow. This is the only boundary condition that can be applied for a well posed computation of flow through a sidewall without modeling the interior channel. Thus, the continuous ingestion modeled a mass sink within the structure.

This simulation also included an approximation of the geometry features located in the RCC channel which are exposed to the external flow by the missing panel since debris forensics obtained during the investigation indicated that these features were present during the reentry. As shown in Figure 20, the geometry modeled in the cavity extended to the main wing spar while retaining the vertical spanner bars and both windside and leeside carrier panels. As a result, an interior cavity is formed within the gap of the missing RCC panel. An additional detail modeled by this simulation was to maintain the width of the outboard RCC rib. An ingestion area of about 312 square inches resulted after this rib surface was included in the geometry.

The full scale computation was performed on a grid with 2 million cells where over half a million cells were located in the cavity. Figure 21 shows the grid on the external potion of the Orbiter as well as the grid within the cavity. The midbody section of the common baseline volume grid (Alter, 2003), shown in black, was modified for inclusion of the cavity grid leaving the nose and aft sections untouched. The midbody section utilized an embedded O-grid topology for the focusing of grid points near the wing leading edge breach. An embedded C-grid topology was used inside the cavity of the missing RCC panel 9 because this topology enables the accurate capture of the carrier panels, spanner bars, and earmuffs. Viscous spaced grids were placed against each surface so that heating computations in the cavity could be captured accurately. The O-C interface at the orbiter OML surface was preserved from the OML so that parametrics with and without the missing RCC panel 9 could be performed.

Figure 22 shows a cross-section of the flow field density in the planform plane for the region surrounding RCC panel 9. Results for both the smooth OML geometry and the case of missing RCC panel 9 are shown. The location of the shock-shock interaction is again evident on the smooth OML as the region of higher density. The inboard corner of Panel 9 is at the shock-shock interaction region. The boundary layer height approaching the cavity varied form 0.65 at the leading edge to 1.4 at the inboard windside corner. The unit Reynolds number varied from 6400/ft at the wing leading edge to 6700/ft at the inboard windside corner of the cavity. The contours of the density approaching the cavity are identical between the two solutions as expected. A complex shock structure is observed in the cavity of the missing panel. At the upstream edge of the cavity an expansion emanates into the shock layer, accelerating and turning the flow into the gap. A weak recompression wave, also emanating from the upstream

edge of the cavity, processes the overexpanded flow. On the outboard RCC rib, an embedded bow shock forms with one-half of the wave ingested into the RCC channel and the other half forming a second interaction with the wing bow shock downstream of the gap. The effects of this interaction appear to be very minor since the intersection angles of this secondary interaction are small and the incident bow shock is already weakened by ingestion of the flow into the RCC channel. The shock layer thickness is approximately 20% smaller over the wing downstream of the missing panel due to the flow ingestion.

A view of the missing panel gap is presented in Figure 23 to illustrate the major surface and flow field features in the cavity. Color contours in the figure represent surface pressures, while the volume streamlines are plotted to indicate flow direction. The streamlines illustrate that a substantial part of the flow entering the missing panel cavity also continues directly into the RCC channel. An attachment line is formed on the outboard RCC rib that separates flow going into the RCC channel from flow continuing onto the wing upper surface. The interior cavity, formed by the presence of upper and lower carrier panels and the spanner bar, produced additional flow features of note in this simulation. Streamlines that flow into this cavity region are deflected toward the wing spar by the spanner bar (away from the RCC channel). A circulation is formed within the volume encompassed by the interior cavity and the leeside of the inboard sidewall. This recirculating flow is “spun” out of the top of the missing RCC cavity into the leeside flowfield.

Predicted heating rates to surfaces in the interior missing RCC panel area are presented in Figure 24. The heating contours closely follow the pressure contours shown in the previous figure except on the exposed edge of the lower carrier panel. It appears that heating in this area is elevated due to a thin boundary-layer and high shear stresses which results in the highest heating rate observed. The heating predicted in this region and on the outboard rib are approximately 300 BTU/ft2/s however it is unclear if the grid is resolved enough to accurate predict the heating on these edges. The heating to the spar is 110 BTU/ft2/s, approximately 3 times the peak heating on the wing leading edge.

A simple view of the streamlines emanating from the leeside of the missing RCC panel gap is shown in Figure 25. The streamline patterns illustrate that the flow leaving the gap corner nearest the inboard sidewall and spar is directed inboard. Flow leaving the gap from other locations along the spar and toward the outboard corner is increasingly turned downstream. The end result is a small area of flow diverted low and toward the side fuselage in this simulation.

Temperature contours normal to the vehicle axis are shown in Figures 26 to 29 for both the smooth OML and the missing RCC panel 9 solutions. The first figure (Figure 26) shows the temperature contours at X = 1051 inches which is 40 inches upstream of the missing RCC cavity. The contours are symmetrical showing that the cavity has no effect on the flow at that station. As this station is within a region of the volume grid which was modified significantly to incorporate the cavity grid, it also shows that the modification of the baseline grid did not result in differences in the computations. Figure 27 shows the temperature contours at X = 1091 inches which corresponds to the inboard corner of the cavity. The missing RCC panel 9 solution produces a jet of hot gas which exits the cavity and scrubs the leeside of the wing in the direction of the fuselage. At this station however, the side of the fuselage appears unaffected by the jet. Figure 28 shows the temperature contours at X = 1204 inches, halfway between the cavity and the OMS pods. At this station, the jet from the cavity has been turned downstream and scrubs the side of the fuselage with the highest temperature gas near the intersection of the fuselage and the wing. Figure 29 shows the temperature contours at X = 1316 inches, at the forward portions of the OMS pods. The jet along the side fuselage remains present at this station although it is cooler. A region of off nominal low temperature is also evident on the leeside surface of the wing for this missing RCC panel 9 solution. The most predominant feature, however, is the high temperature gas on the surface of the OMS pods. While both the baseline smooth OML solution and the missing RCC panel 9 solution show hot gases in this region, a higher temperature gas occurs for the baseline solution noted by the white levels in the contour.

The effect of the flow jetting over the wing and side fuselage can be seen in Figure 30 which shows the difference in the pressure coefficient due to the missing RCC panel 9 with ingestion. The shows an increased pressure on the side fuselage near the wing-body juncture. The damage, however, does not produce a load on the left side of the vertical tail which was thought a possible explanation for the positive rolling moment observed on the Orbiter reentry.

The effect of the leeside flow field perturbation shown in figures 26 to 29 can also be seen in Figure 31. Here the amplification of heating rate relative to the baseline (undamaged geometry) is plotted to isolate the effects of the missing RCC panel. As would be expected from the streamline patterns, the fuselage heating is increased in the area where the flow diverted through the missing panel gap strikes the fuselage. In this case, the heating augmentation pattern assumes a horizontal orientation and is confined near the wing-fuselage juncture. Augmentation factors as high as 2.75 over the nominal heating case are predicted on the fuselage. The effect on the OMS Pod is opposite in that lower heating levels (0.5 times) are predicted for the missing panel solution relative to the baseline. The results of other simulations (both CFD predictions and wind tunnel measurements) with missing RCC panels (both 6 and 9) have shown similar trends, but quantitatively different heating patterns. In those cases, the heating augmentation on the fuselage is larger, occurs more upstream and higher on the side of the fuselage, and the pattern assumes an angled orientation. Also, heating to the OMS pod in those cases generally increased.

The effect of the increased heating rate on the equilibrium surface temperature is presented in Figure 32. Here, the absolute difference in temperature between the nominal and missing RCC panel solution is shown. The peak temperature produced on the side fuselage for the damaged case is 408 deg F; however, peak temperatures of 1450 deg F are observed on the leeside wing near the inboard corner of the cavity.

As this solution requires supersonic ingestion into the wing channel or through the spar, it is probably not an appropriate model prior to large spar penetration, which according to the Columbia Accident Investigation Board (CAIB report 2003) could have occurred as early as 487 seconds EI. It may, however, be appropriate at later times and could account for the movement of the heating signature on the side fuselage seen at 620 seconds EI (Figure 33) noted by the reduction in the off nominal high values of the two side fuselage surface thermocopuples (CAIB report, 2003).

Comparison of RCC 6 and RCC 9 Solutions

A comparison of the heating augmentation computed for the missing RCC panel 6 “notch” and the missing RCC panel 9 with ingestion is shown in Figure 34. The heating augmentation is plotted on the same scale to aid in comparison. It is clear that the heating augmentation is more significant for the missing RCC panel 6 notch solution than for the missing RCC panel 9 solution with ingestion. In addition, the heating footprint on the side fuselage has moved off the side fuselage onto the wing fuselage juncture for the missing panel 9 solution. From parametric wind tunnel measurements of missing RCC panels (Horvath, 2003), a trend was observed which indicated that the fuselage heating signature tended to become more horizontal for panels further outboard. This trend is also observed in the differences between the panel 6 and 9 computations. However, wind tunnel measurements showed that the horizontal heating footprint remained high on the side fuselage for all outboard missing RCC panels unlike the prediction obtained for missing panel 9. Movement of the heating signature to the lower side fuselage in the computation is believed due to the effect of the ingestion flow into the RCC channel and possibly by the presence of the interior cavity. The streamlines indicate that the closed cavity of RCC panel 6 notch acted to redirect the flow onto the side fuselage while the streamlines for the missing RCC panel 9 with ingestion show that the majority of flow that enters the cavity gets ingested. Only a small portion of the flow strikes the interior cavity sidewalls (spanner bars) and gets spun out of the inboard edge of the cavity to eventually hit the fuselage-

wing juncture region. Thus, the momentum difference between these two damage configurations of the flows exiting the cavity on the leeside is believed to be the determining factor in the penetration of the jet into the leeside flowfield and onto the side fuselage.

Conclusions

Each of the computations, for the missing RCC panel 6 notch and the missing RCC panel 9 with ingestion, reproduce heating trends which were observed at different times in the STS-107 re-entry trajectory. The missing RCC Panel 6 "Notch" solution showed slanted heating footprint and an augmentation of 5 times the nominal heat flux on the left side fuselage. A comparison with measurements from a similar test in the CF_4 wind tunnel showed a general agreement with this prediction in terms of both location and orientation. The missing RCC panel 9 solution with continuous ingestion into the RCC channel shows a horizontal heating footprint confined near the wing-fuselage juncture. Heating augmentation values up to 2.75 times the nominal heat rate are predicted on the fuselage and cooling factors of 0.5 on the OMS pod. No wind tunnel data with continuous ingestion was available for comparison. The more horizontal nature of the missing RCC panel 9 heating footprint is believed due to the more outboard position of the lost tile. The reduction and movement of the heating augmentation lower on the side fuselage is believed due to the effect of mass ingestion into the RCC channel and possibly the interior cavity. For the closed cavity of RCC panel 6 notch, the flow entering the cavity was redirected onto the side fuselage while for the missing RCC panel 9 with ingestion, the majority of flow entering the cavity gets ingested with only a small portion being redirected to strike the fuselage-wing juncture region. Thus the momentum difference of the flow exiting the cavity for these two damage configurations is believed to be the determining factor in the penetration of the jet into the leeside flowfield and onto the side fuselage. The results from the missing RCC panel 6 solution are consistent with a heating increase on the side fuselage observed from the MADS data between 560 and 620 EI. The missing panel 9 solution models continuous ingestion into the wing channel. As such it is probably not an appropriate model prior to spar penetration. It may however, be appropriate at later times and could account for the reduction in heating augmentation on the side fuselage seen at 620 EI.

References

Alter, S.J. (2003), McDaniel, R.D., and Reuther, J.J., "Development of a Flexible Framework of Common Hypersonic Navier-Stokes Meshes for the Space Shuttle Orbiter," JANNAF Conference, 2003

Bibb, K.L.(2003), and Prabhu, R.K., "Computational Aerodynamic Characteristics of Shuttle Orbiter for Range of Damage Scenarios at Hypersonic Flight and Wind Tunnel Conditions," JANNAF Conference, 2003

Brauckmann, G.J.(2003), and Scallion, W.I., "Experimental Hypersonic Aerodynamic Characteristics of the Space Shuttle Orbiter for a Range of Damage Scenarios," JANNAF Conference, 2003

Buck, G.M. (1989), "Automated Thermal Mapping Techniques Using Chromatic Image Analysis," NASA TM 101554.

"Columbia Accient Investigation Report", Report Volume I, August 2003

Everhardt, J.L.(2003), Bey, K.S., Wood, W.A., and Pulsonetti, M.V., "Experimental and Computational Investigation of Cavity Flow Simulating Debris Damage to Thermal Protection System Tiles," JANNAF Conference, 2003

Gnoffo, P.A. (1989), Gupta, R.N., and Shinn, J., “Conservation Equations and Physical Models for Hypersonic Air Flows in Thermal and Chemical Nonequilibrium,” NASA TP 2867.

Gnoffo, P.A. (1990), “An Upwind-Biased, Point-Implicit Relaxation Algorithm for Viscous, Compressible Perfect-Gas Flows,” NASA TP 2953

Horvath, T.J. (2003), “Experimental Aeroheating Characteristics of the Space Shuttle Orbiter for a Range of Damage Scenarios,” JANNAF conference, 2003.

Merski, N.R. (1998a), “Reduction and Analysis of Phosphor Thermography Data With the IHEAT Software Package,” AIAA Paper 98-0712.

Merski, N.R. (1998b), “Global Aeroheating Wind-Tunnel Measurements Using Improved Two-Color Phosphor Thermography Method” *Journal of Spacecraft and Rockets*, Vol. 36, No. 2, pp. 160-170.

Stewart, D.A. (1997), “Surface Catalysis and Characterization of Proposed Candidate TPS for Access-to-Space Vehicles,” NASA TM 112206.

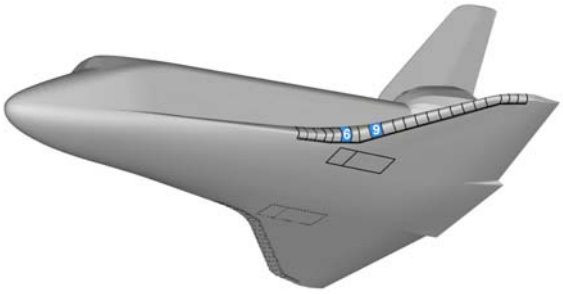

Figure 1. Baseline Orbiter Geometry with RCC panels Labeled

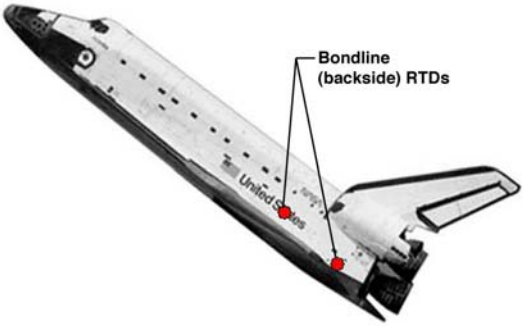

Figure 2. Bondline (backside) Resistance Temperature Detectors (RTD's) on Orbiter Left Side Fuselage

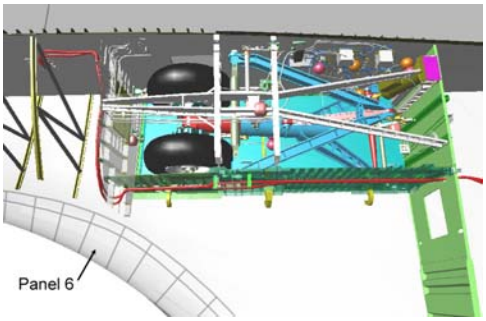

Figure 3. Orbiter Port Wing Wheel Well

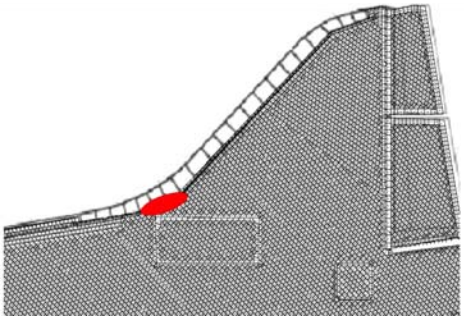

Figure 4 Early Prediction of Foam Impact Region

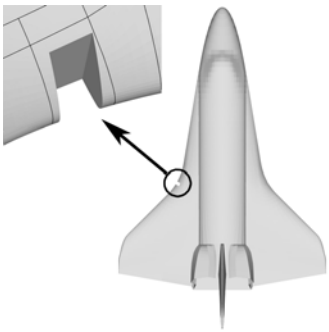

Figure 5. Geometry for RCC Panel 6 "Notch"

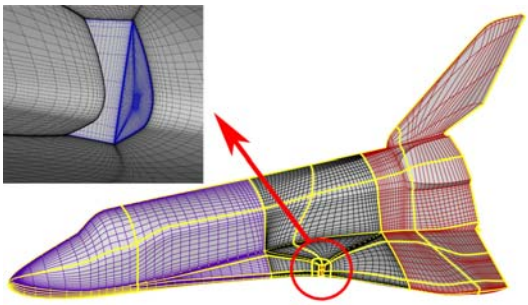

Figure 6. Grid about the Orbiter and in the Vicinity of Panel 6 Notch

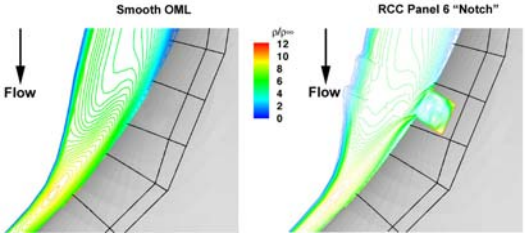

Figure 7. Comparison of Density Contours in Missing RCC Panel 6 "Notch" Cavity and on Smooth OML Baseline Grid

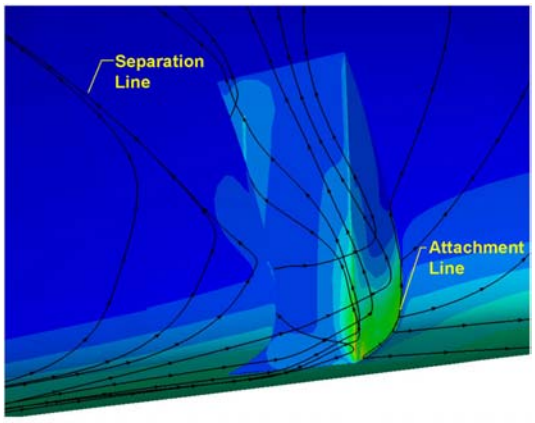

Figure 8. Streamlines in RCC Panel 6 "Notch" Cavity.

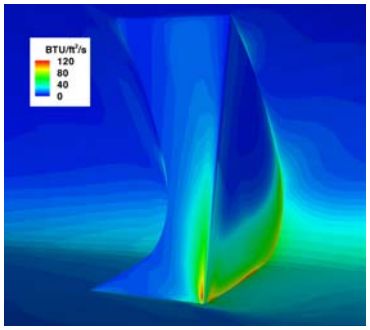

Figure 9. Heat Flux Contours in RCC Panel 6 “Notch”

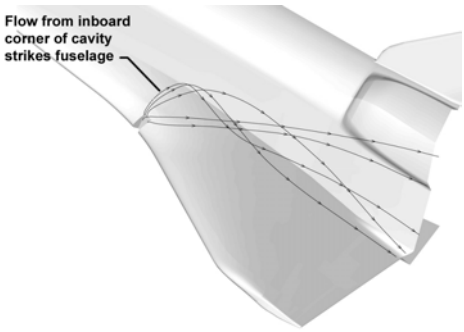

Figure 10. Streamlines on the Body Emanating from the RCC Panel 6 “Notch”

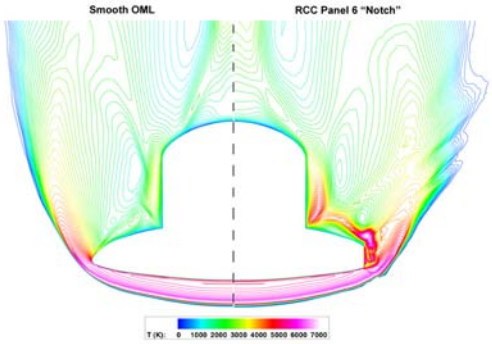

Figure 11. Temperature Contours at X = 1036 inches (through panel 6 notch)

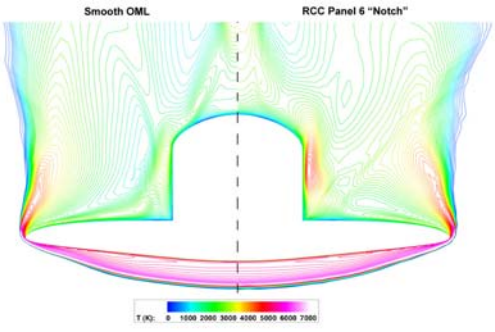

Figure 12. Temperature Contours at X = 1181 inches (halfway between notch and OMS pods)

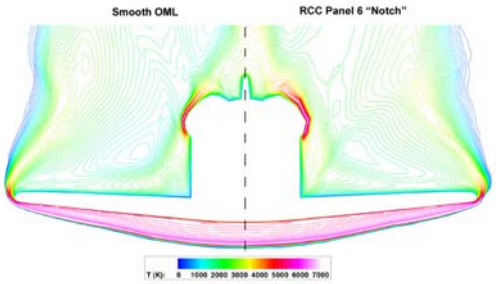

Figure 13. Temperature Contours at X = 1326 inches (forward face of OMS pod)

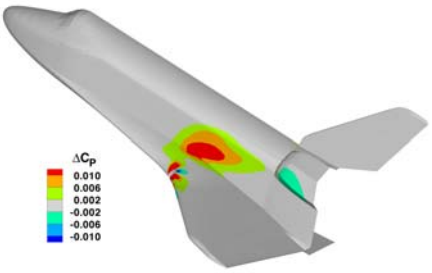

Figure 14. Difference in Pressure Coefficient due to Missing RCC Panel 6 “Notch”

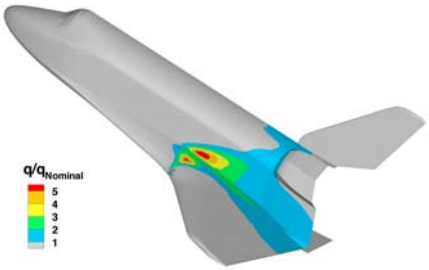

Figure 15. Heating Augmentation due to Missing RCC Panel 6 “Notch”

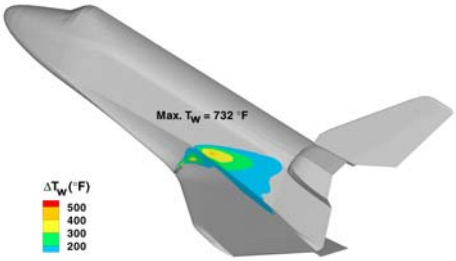

Figure 16. Surface Temperature Increase due to Missing RCC Panel 6 “Notch”

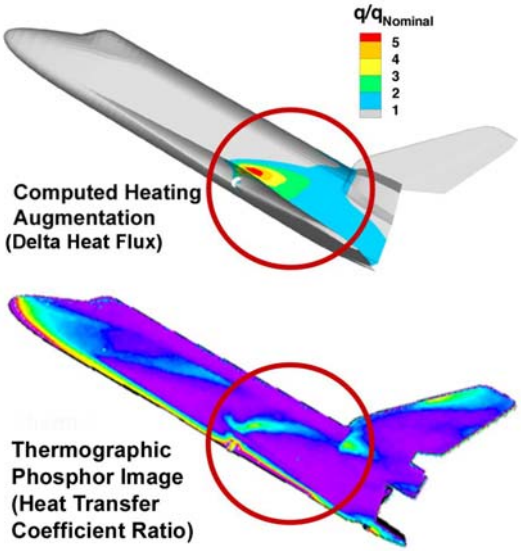

Figure 17. Qualitative Comparison of Computed Heat Flux Augmentation with Wind Tunnel Heating Measurements.

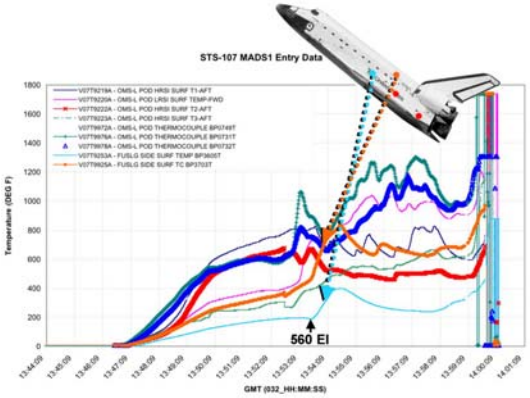

Figure 18. STS-107 MADS Re-Entry Thermocouple Data on the Left Side of the Fuselage and on the Left OMS POD with Times Relevant to the Missing RCC Panel 6 "Notch" Solution

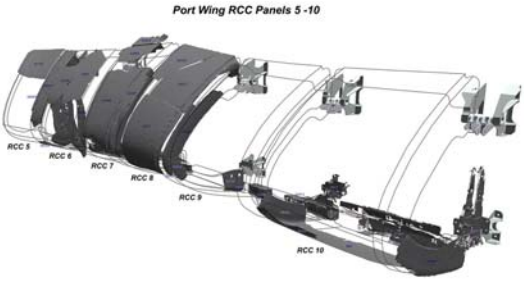

Figure 19. Debris Recovered in the Vicinity of RCC Panel 9

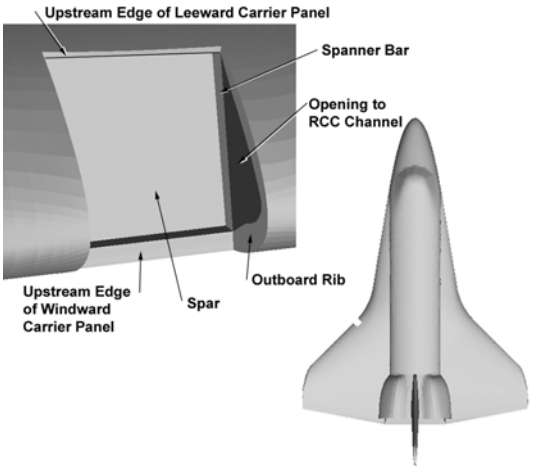

Figure 20. Geometry for Missing RCC Panel 9 with Mass Ingestion in RCC Chamber

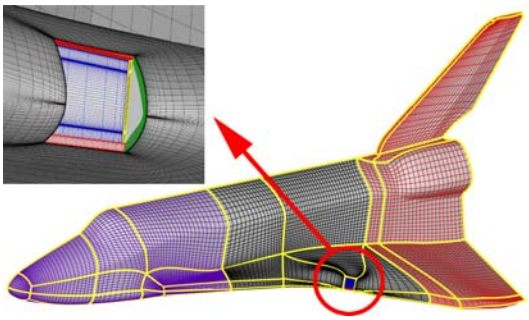

Figure 21. Grid about the Orbiter and in the Vicinity of Missing RCC Panel 9 Cavity.

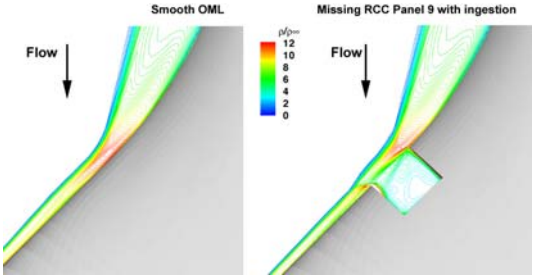

Figure 22. Comparison of Density Contours in Missing RCC Panel 9 Cavity and on Smooth OML Baseline Grid

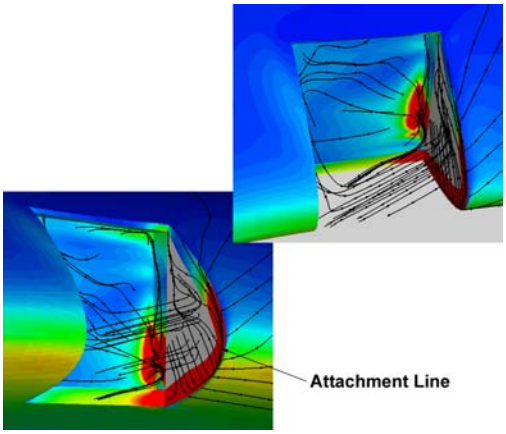

Figure 23. Pressure Contours, Volume Streamlines and Surface Streamlines in Missing RCC Panel 9 Cavity with Ingestion

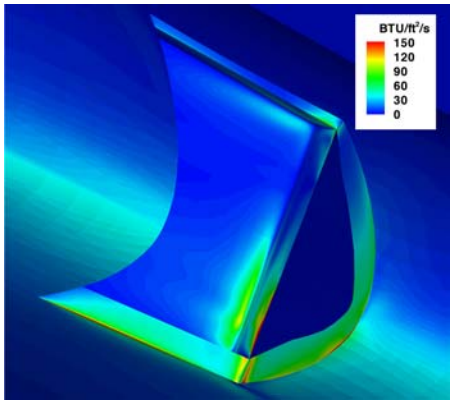

Figure 24. Heat Flux Contours in the Missing RCC Panel 9 Cavity with Mass Ingestion

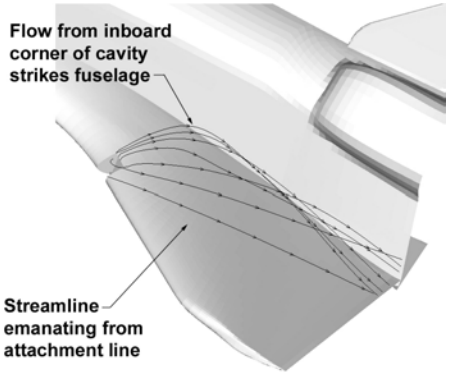

Figure 25. Streamlines on the Body Emanating from the RCC Panel 9 Cavity

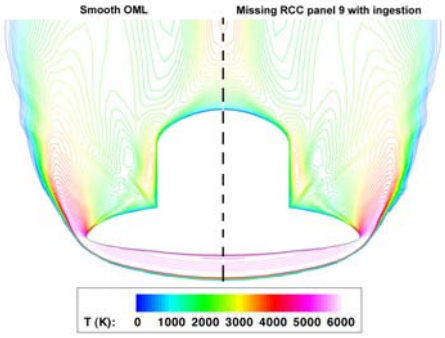

Figure 26. Temperature Contours at X = 1051 inches (40 inches upstream of RCC Panel 9 Cavity

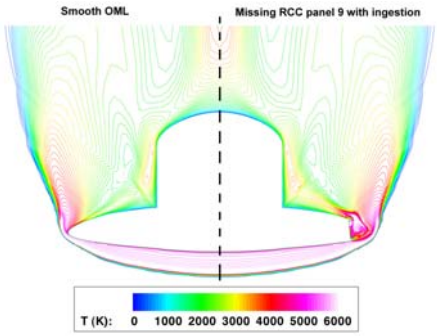

Figure 27. Temperature Contours at X = 1091 inches (at inboard corner of cavity)

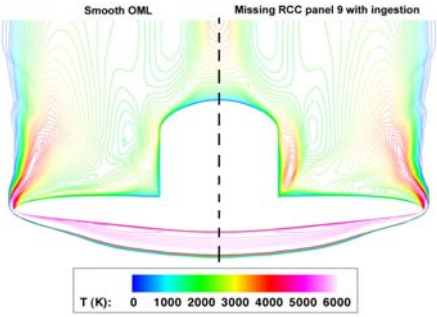

Figure 28. Temperature Contours at X = 1204 inches (halfway between cavity and OMS pods)

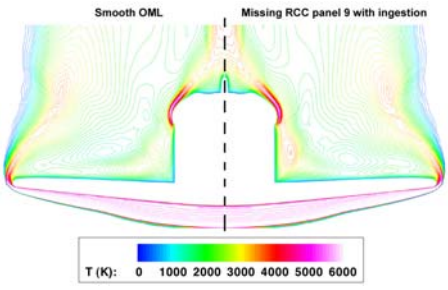

Figure 29. Temperature Contours at X = 1316 inches (at forward portions of OMS pods)

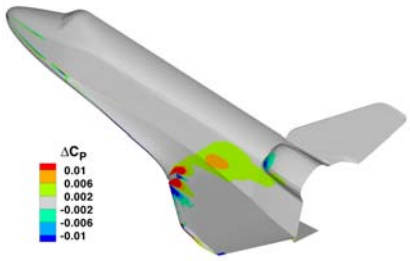

Figure 30. Difference in Pressure Coefficient due to Missing RCC Panel 9 with Mass Ingestion

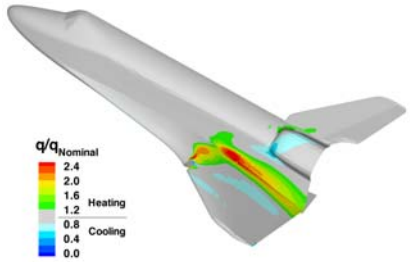

Figure 31. Magnification Factor for Missing RCC Panel 9 Heat Flux with Mass Ingestion

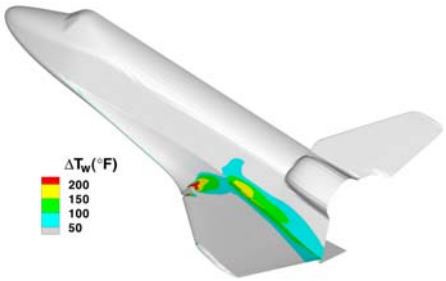

Figure 32. Surface Temperature Increase due to Missing RCC Panel 9 with Mass Ingestion

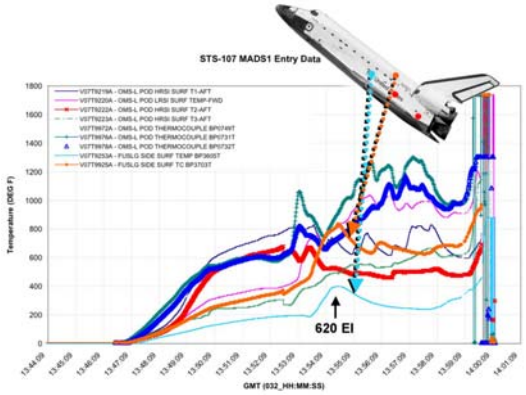

Figure 33. STS-107 MADS Re-Entry Thermocouple Data on the Left Side of the Fuselage and on the Left OMS POD with Times Relevant to the Missing RCC Panel 9 Solution with Continuous Mass Ingestion

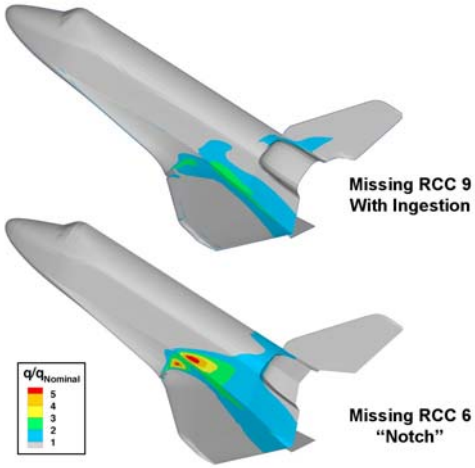

Figure 34. Comparison of Missing RCC Panel 6 "Notch" and Missing RCC Panel 9 with Mass Ingestion Computations.